The Impact of Sb and Na Doping on the Surface Electronic Landscape of Cu2ZnSnS4 Thin-films

Journal:	*ACS Energy Letters*
Manuscript ID	nz-2018-02081e.R1
Manuscript Type:	Letter
Date Submitted by the Author:	11-Nov-2018
Complete List of Authors:	Tiwari, Devendra; University of Bristol, School of Chemistry Cattelan, Mattia; University of Bristol School of Chemistry, Harniman, Robert; University of Bristol, Department of Chemistry Sarua, Andrei; University of Bristol, School of Physics Fox, Neil; University of Bristol, Chemistry Koehler, Tristan; University of Duisburg-Essen Klenk , Reiner; Helmholtz-Zentrum Berlin fur Materialien und Energie GmbH Fermin, David; University of Bristol, School of Chemistry

The Impact of Sb and Na Doping on the Surface Electronic Landscape of Cu_2ZnSnS_4 Thin-Films

*Devendra Tiwari,[a] Mattia Cattelan,[a] Robert L. Harniman,[a] Andrei Sarua,[c] Neil Fox,[b,c] Tristan Koehler,[d] Reiner Klenk[e] and David J Fermin[a]**

[a]School of Chemistry, Cantocks close, University of Bristol, Bristol BS8 1TS, United Kingdom

[b]Nanoscience and Quantum Information Centre (NSQI), 5 Tyndall Ave, Bristol BS8 1FD, United Kingdom

[c]H.H. Wills Physics Laboratory, School of Physics, University of Bristol, Tyndall Avenue, Bristol BS8 1TL United Kingdom

[d]Faculty of Physics, University of Duisburg-Essen, Forsthausweg 2, 47057 Duisburg, Germany

[e]Helmholtz-Zentrum Berlin für Materialien und Energie, Hahn-Meitner-Platz 1, D-14109 Berlin, Germany

*David.Fermin@bristol.ac.uk

Abstract

Open circuit voltage deficiency is the key limiting factor in Cu_2ZnSnS_4 (CZTS) thin-film solar cells, which is commonly associated with band tails and deep gap states arising from elemental disorder. The introduction of dopants such as Na and Sb has led to improvement in device performance, yet their effects on the opto-electronic properties of CZTS are yet to be fully elucidated. In this letter, we unraveled the effect of Sb and Na:Sb co-doping on the surface energy landscape of solution processed CZTS employing energy-filtered photoelectron emission microscopy. In the absence of the additives, 150 nm resolution photoemission maps reveal oscillations in the local effective work function as well as areas of low photoemission energy threshold. The introduction of dopants substantially reshapes the photoemission maps, which we rationalize in terms of Cu:Zn and Sn disorder. Finally, we establish unprecedented correlations between photoemission landscape of thin films and the performance of over 200 devices.

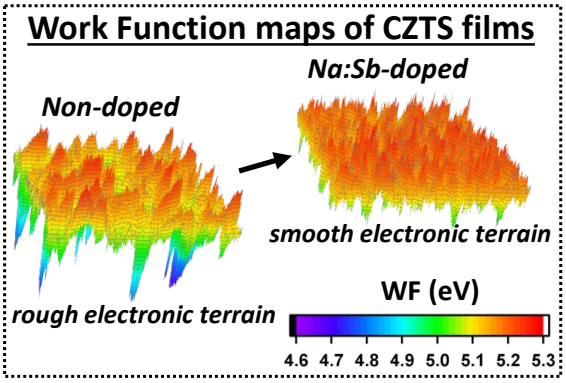

$Cu_2ZnSn(S,Se)_4$ (CZTSSe) solar cells have delivered certified power conversion efficiency of $\eta = 12.7\%$, which is the highest in the context of Earth-abundant inorganic thin-film solar cell technology.[1] Over the last six years, breaking this record efficiency has been a key driver for a large community of material scientists.[2–4] The structural, optoelectronic properties of CZTSSe are closely related to those of $CuInGa(S,Se)_2$ (CIGSSe).[5] However, CIGSSe has achieved record efficiency close to 23%, employing the same general device architecture.[6] The record efficiency of the pure sulfide form (CIGS) is close to 15.5%,[7] while Cu_2ZnSnS_4 (CZTS) is limited to 8.17% in the case of solution processed films[2,8] and 11.01% recently obtained by physical vapor deposition.[9] There is a clear consensus that the performance gap between these two sets of materials is mainly connected to the voltage generation. An improvement of the open-circuit voltage of CZTSSe cells by a factor of two will set the basis for a new and sustainable technology based on Earth-abundant elements with the potential of boosting the current footprint of thin-film technology in the PV market.[10]

Voltage losses in CZTSSe are often linked to structural disorder which manifests itself as band tails and deep trap states.[11,12] Cu-Zn antisite is the main type of defect contributing to band tails, while Sn disorder generates energy levels deep in the band gap.[13–15] In addition, secondary phases including binary (chalcogenides), ternary (Cu_2SnS_3) and quaternary (I-42m phase, i.e. stannite) compounds can also co-exist along with the main I-4 (kesterite) phase.[16–23] *These defects are expected to limit device performance, although little is known about the extent by which they affect specific metrics such as the open circuit voltage* (V_{OC}). Two general strategies have been implemented to minimize structural disorder: (i) Tuning annealing conditions, often under SnS excess. to drive the reaction towards the quaternary phase[24,25] and (ii) introducing dopants such as Na, Sb, Ag, Cd and Ge which can aide crystallization and decrease elemental disorder.[26–35] The vast majority of these studies correlates the effect of

dopants on bulk structural properties and device performance. However, no knowledge has been gathered on the effect of dopants on the surface electronic properties of these materials.

In this report, the complex surface electronic landscape of CZTS films prepared by solution-based methods is unveiled by energy-filtered photoemission electron microscopy (EF-PEEM), focusing on the effect of Sb and Na:Sb doping. This technique enables resolving photo-emission spectra with 150 nm lateral spatial resolution, generating highly detailed local effective work-function (LEWF) maps. This information, supported by atomic force microscopy, Raman microscopy and DFT calculations uncovers new correlations between surface electronic properties and device performance. Our studies are supported by a statistical analysis of Sb and Na:Sb doping on CZTS devices carried over hundreds of cells.[28] We provide conclusive evidence that Sb decreases Sn disorder, which can be linked to device shunting paths. On the other hand, Na:Sb co-doping decreases Cu:Zn disorder, tuning carrier density and improving cell voltage.

The performance of representative CZTS solar cells with the architecture glass/Mo (500 nm)/CZTS (1.35 μm)/ CdS (60 nm)/ i-ZnO, Al:ZnO (430 nm)/Ni:Al is ilsutrated in **Figure 1**. CZTS films were prepared by thermolysis of molecular precursors deposited by spin-coating following previously reported procedures, with Na and Sb are added to the precursor solution.[28] Further details on the preparation and characterization of CdS thin-film and devices are provided in the supplementary information (**S1**). Characteristic *J-V* curves in **Figure 1a** show that the V_{OC} and fill factor (*FF*) improves upon doping, while the short circuit current (J_{SC}) remains effectively constant around 15 mA.cm^{-2}. The somewhat attenuated J_{SC} value is connected to reflections losses and the rather thick CdS layer employed in our studies. These effects are evident in the external quantum efficiency (EQE) spectra in **Figure 1b**, showing a maximum value close to 70% and strong attenuation at wavelengths below 550 nm. In our previous study involving over 216 cells, we concluded that the mean η values of non-doped

CZTS increase from 3.2 to 4.7 and 5.05 % upon doping with Sb and Na:Sb, respectively, with the champion cell performance of 5.72%.[28]

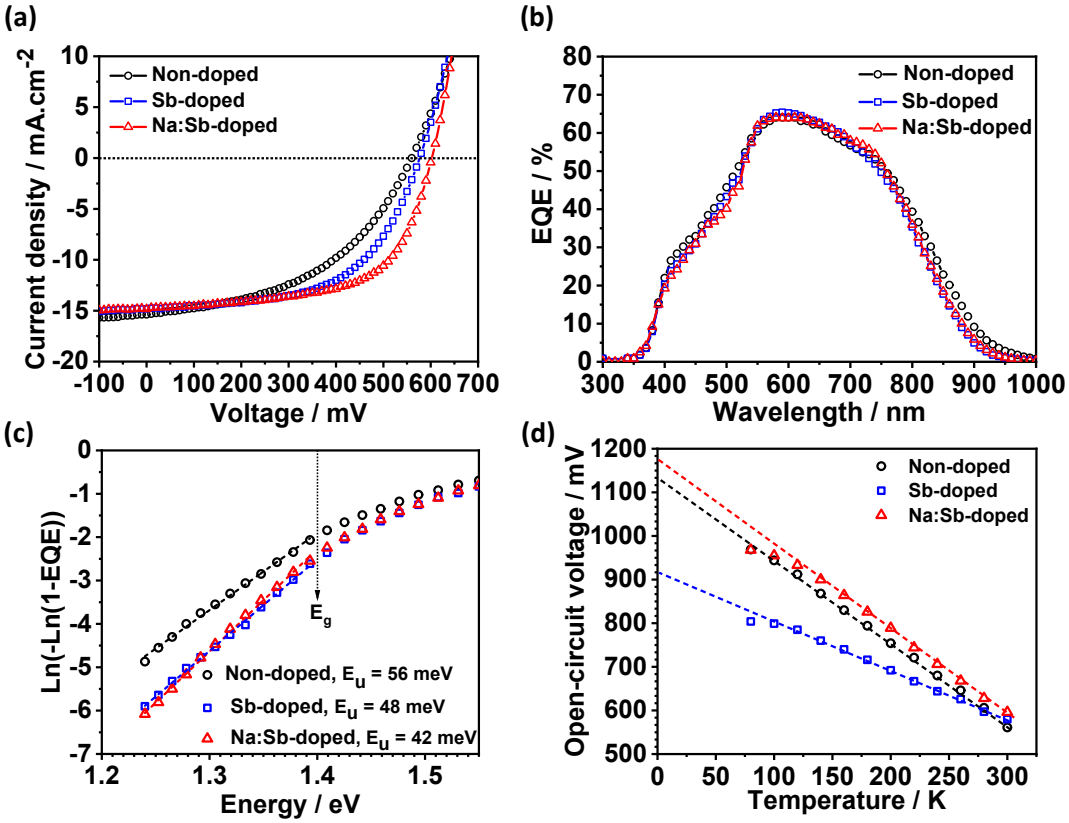

Figure 1: CZTS solar cells performance: (a) Current-Voltage characteristics under simulated AM 1.5G illumination, (b) external quantum efficiency (EQE) spectra, (c) estimation of Urbach tail energy from sub-bandgap EQE and (d) temperature dependence of open-circuit voltage (V_{OC}). The low-temperature intercept in (c) is used for establishing the activation energy ($E_{A,Voc}$) of the predominant recombination pathway.

Further information on loss mechanisms can be obtained by estimating Urbach tail energies (E_U) from the EQE onset wavelength, as well as the temperature dependence of V_{OC} (Figures **1c** and **1d**, respectively). Following the formalism introduced by Troviano and Taretto (see also section **S1**),[36] a systematic decrease of E_U values from 56 ± 2.2 to 42 ± 1.2 meV is observed upon doping. This trend is consistent with decreasing elemental disorder and the overall improvement of device performance. The E_U values are within the range of those

reported for record efficiency CZTS cells.[4,12,27] The activation barrier ($E_{A,Voc}$) of the predominant recombination mechanism is calculated from extrapolating the temperature dependence of V_{OC} (see section **S1**), resulting in values smaller than the band gap (E_g = 1.4 eV) in doped and undoped samples. These trends point towards interfacial recombination as key in device performance. Key device metrics as well as E_U and $E_{A,Voc}$ as a function doping are summarised in the supporting information **Table S1**.

Photoemission analysis of CZTS was performed on films etched in KCN just before being introduced into the UHV chamber. Details of the experimental procedure and instrumentation are provided in the supplementary information (**S2**). Carbon and oxygen impurities were minimized by exposing the film to low doses of Ar plasma. **Figures S1** to **S3** display survey XPS data of non-doped and doped samples, highlighting the suppression of the C 1s and O 1s signals after the Ar pre-treatment. Judicious adjustment of the Ar pre-treatment ensured that the surface metal ratio remains largely unaffected as shown in **Table S2**. All the three films have similar Zn-rich and Cu-poor stoichiometry which has been identified as optimal for high-performance CZTS solar cells.[37] The surface [Zn]/[Sn] ratio (around 1.3) is similar to the bulk ratio (~ 1.4) estimated from EDX, while the [Cu]/([Zn]+[Sn]) ratio at surface (0.50 to 0.57) is significantly lower than in the bulk (~ 0.78) as a result of the KCN etching. No clear Sb 3d signal is detected in any of the doped samples, suggesting that the surface concentration of the dopant is below the detection limit. It should be mentioned that the detection of Sb 3d is complicated by the overlap with O 1s. Interestingly, secondary ion mass spectrometry (SIMS) depth profile shows the preferential segregation of Sb at the Mo/CZTS boundary as shown in **Figure S4**. Similar elemental profile has been reported in Sb doped CIGS films.[38] Wavelength dispersive X-ray spectrometry (WDS) analysis of the rear-side of the CZTS films exposed by peeling the films off the substrate with adhesive epoxy show Sb content below 0.07 wt% (**Table S1**).

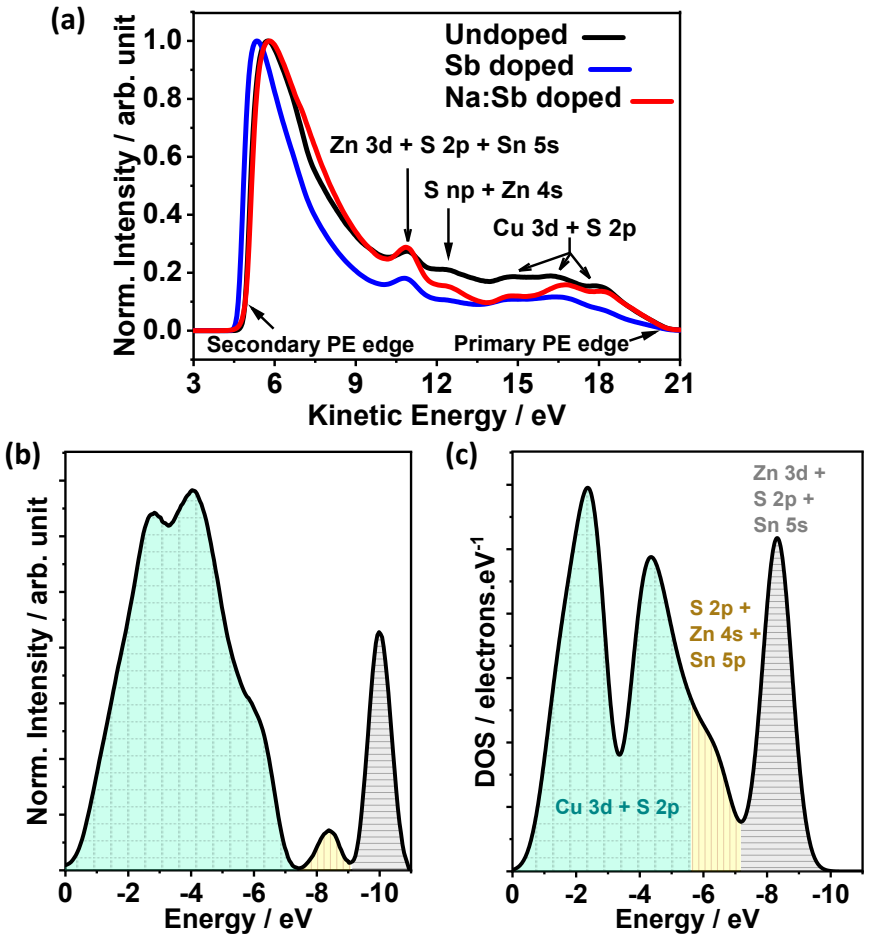

Figure 2: CZTS photoemission spectra under 21.2 eV He(I) illumination: (a) photoemission spectra of non-doped and doped CZTS films featuring the primary (high energy) and secondary (low energy) photo-electron emission thresholds; (b) valence band spectrum of Na:Sb-doped CZTS films plotted with binding energy scale and after applying a Tougaard background subtraction; (c) valence band density of states (DOS) calculated for Cu_2ZnSnS_4 using HSE06 functional. A Gaussian smearing of 0.4 eV is employed to match the broadening in the experimental measurements.

The films were transferred from the XPS to the EF-PEEM chamber (Focus Gmbh NanoESCA II) under UHV, with characteristic photoemission spectra of the non-doped and doped CZTS films illustrated in **Figure 2a**. The features associated with the valence band spectrum can be observed towards the *primary* energy threshold.[39,40] **Figure 2b** shows the valence band spectrum of the Na:Sb-doped sample after subtracting the photoemission background using a Tougaard function. The features can be rationalized by examining the

density of states of CZTS calculated by DFT HSE06 functional shown in **Figure 2c**. The computational approach is described in the supplementary information (**S3**). The calculations reproduce key features associated with valence Cu 3d, Sn 5s + 4p, Zn 3d and S 2p bands. The contributions from the various orbitals to the valence band DOS along with further details of the DFT calculations are found in the supplementary information (**Figure S5**). A shift in the Zn 3d emission line can be observed between the experimental and computed DOS, along with slight differences in the line shape of the Cu 3p band. These differences can be linked to the off-stoichiometric composition of the films compared to the supercell used in the calculations. In any case, *we can conclude that the valence band spectra of the films are essentially dominated by the main CZTS phase*.

Figure 3a-c show the distribution of the *secondary* energy threshold of electron photoemission obtained from fitting an error function to local spectra recorded at 150 nm spatial resolution. The low energy photoemission threshold in smooth single crystal facets can be defined as the *work function*. In our discussions, we adopt the term local effective work function (LEWF) in view of the polycrystalline nature of CZTS thin-films as well as potential contributions from local topography and surface inhomogeneities. The maps unraveled a complex energy landscape characterized by fluctuations in LEWF values around a mean value. The effect of dopants on the LEWF can be visualized by the histogram shown in **Figure 3d-f**. The maximum in the distribution is located between 4.8 eV (Sb-doped) and 5.2 eV (Na:Sb-doped). These values are within the range reported in two recent studies based on Kelvin probe force microscopy and UPS.[41,42]

A closer examination of the photoemission maps shows that the non-doped samples exhibit a broader LEWF distribution centered at 5.1 eV, as well as photoemission hot-spots with values as low as 4.6 eV (**Figure 3a** and **3d**). Discrete photoemission hot-spots are likely to be associated with to Sn^{2+} sites,[43,44] which can be responsible for shunting paths in devices.

In our recent study of localized valence band spectral features of CZTSSe films, supported by DFT calculations, concluded that surface confined Sn^{2+} states are responsible for areas of low LEWF.[45] Furthermore, conducting AFM images (**Figure S6)** reveal local points of high current at the non-doped samples, while significantly less contrast is observed in the doped samples. Photoemission hot-spots are substantially attenuated upon Sb doping (**Figure 3b** and **3e**), leading to a narrower distribution of LEWF. Sb^{+3} is expected to occupy Sn sites in CZTS given the similar ionic radius to Sn^{+4}. Our previous structural analysis has shown that this level of Sb doping decreases the isotropic temperature factors associated with Sn (2b) sites.[28]

Sb doping also generates a substantial decrease in the overall work function with respect to non-doped films, which can be rationalized by the promotion of donor states. A similar effect has also been observed in Sb-doped CIGS thin-films.[46] Duan et al. proposed that low doping levels of Sb generate deep states which could be detrimental to the device performance,[26] however this effect appears to be counter-balanced by a decrease in Sn disorder which improve V_{OC} and fill factor. Upon Na:Sb co-doping (**Figures 3c** and **3f**) the mean LEWF is increased to 5.2 eV while keeping the same narrow distribution observed in the case of only Sb doping. The introduction of Na^{+} leads to isoelectronic doping of Cu sites,[29] while increasing majority carrier concentration and thus the overall work function.[33,47]

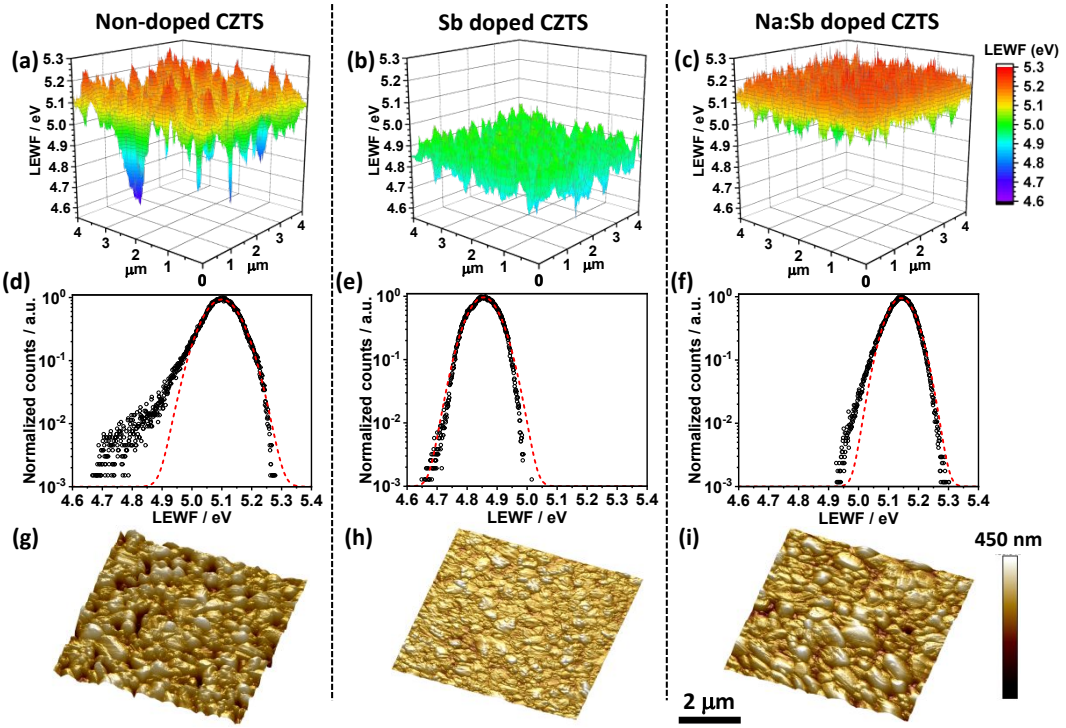

Figure 3: Photoemission and topographic landscape of CZTS films generated by 150 nm resolution EF-PEEM maps: (a-c) Local effective work function (LEWF) maps estimated from the secondary photoemission threshold of non-doped, Sb and Na:Sb co-doped samples; (d-f) corresponding cumulative LEWF histograms displayed in semi-logarithmic scale; (g-i) corresponding atomic force micrographs of non-doped and doped CZTS films.

Fluctuations in the LEWF can be attributed to factors such as compositional disorder, secondary phases, and topographic fluctuations. Fitting Gaussian functions to the distribution of LEWF in **Figures 3d-f** yielded variance values (σ_{LEWF}) of 59, 48 meV and 42 meV for the non-doped, Sb-doped and Na:Sb co-doped CZTS films, respectively. **Figures 3g-i** show characteristic 5 x 5 μm^2 AFM images of the doped and non-doped CZTS films, in which the RMS roughness only differs by 6 nm. Raman spectra, as well as Raman mapping with a 532 nm excitation source (**Figure S7**), do not provide evidence of secondary phases such as Cu_2SnS_3. Indeed, a variation of the A mode (334-338 cm^{-1}) across areas as large as 5 x 5 μm^2 is within the instrument detection limit.[16–18,21,23] These evidences further support the notion that

LEWF fluctuations are related to a microscopic compositional disorder such as Cu-Zn antisite domains, as well as Sn disorder in the case of the non-doped films.

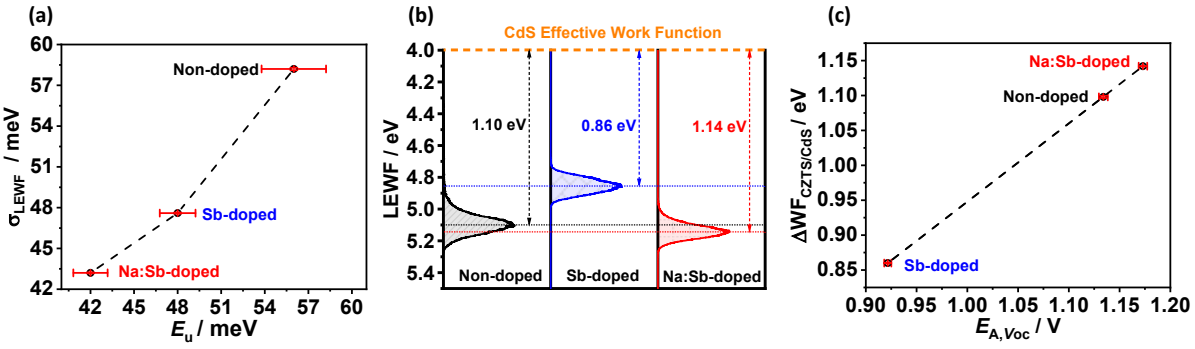

Figure 4: Correlation between CZTS photoemission maps and device performance: (a) LEWF distribution variance (σ_{LEWF}) vs. Urbach energy (E_u) estimated from device EQE spectra; (b) LEWF distribution of non-doped and doped CZTS films vs the effective CdS work function estimated from electrochemical impedance spectroscopy (**Figure S8**), defining the effective barrier height ($\Delta WF_{CZTS/CdS}$); (c) $\Delta WF_{CZTS/CdS}$ vs the activation energy $E_{A,Voc}$ estimated from the temperature dependence of V_{OC}.

The surface electronic landscape of CZTS films uncovered by EF-PEEM exhibits remarkable correlations with device properties as illustrated in **Figure 4**. For instance, the variance of the LEWF modulation closely correlates to the depth of the Urbach band tails as estimated from the EQE spectra (**Figure 4a**). This observation is highly significant, connecting spatial fluctuation of LEWF, Cu:Zn compositional disorder and device performance. While the interpretation of the activation energy $E_{A,Voc}$ for heterojunctions with dominant interface recombination is not trivial,[48] a second correlation can be established experimentally through the effective barrier height ($\Delta WF_{CZTS/CdS}$) defined as the difference between the effective WF of CZTS and CdS. **Figure 4b** illustrates how the $\Delta WF_{CZTS/CdS}$ is affected by the dopant, while **Figure 4c** shows the close match the relation between $\Delta WF_{CZTS/CdS}$ and $E_{A,Voc}$. This correlation, built from three independent experimental measurements, corroborates that mean LEWF of CZTS films provides a strong indication of the maximum device cell voltage. It is important to

consider that the formation of the CZTS and CdS junction leads to elemental substitutions,[49–51] which can affect the surface energy landscape. However, the correlations highlighted in **Figure 4** provide a clear link between the surface electronic properties of the absorber and the whole device performance.

Sub-micron resolution EF-PEEM unravels the subtle role of Sb and Na:Sb doping on the surface energy landscape CZTS film. Non-doped films feature a broad distribution of LEWF around 5.1 eV, along with photoemission hot-spots as low as 4.6 eV which are most probably linked to Sn^{2+}. Sb doping attenuates the low LEWF zones, leading to a narrower distribution of values at around 4.9 eV. Sb interact with Sn sites, decreasing the population of detrimental Sn defects while generating donor states which decreases the overall work function. On the other hand, Na:Sb co-doping promotes not only a narrowing of LEWF distribution (lattice disorder), but also an increase in the overall work-function due to the isoelectronic substitution of Cu^{+} by Na^{+}. We establish unprecedented correlations between the distribution of LEWF and depth of Urbach tails estimated from EQE spectra of devices, as well as between the mean LEWF and the low-temperature limit of the open-circuit potential. These observations suggest that further increasing the effective barrier height $\Delta WF_{CZTS/CdS}$ may lead to improvement in device voltage. However, these should be accomplished by minimizing Sn disorder which is linked to shunting paths across the CZTS/CdS boundary.

Supplementary information

The Supporting Information is available free of charge on the ACS Publications website at DOI:. S1 CZTS thin film preparation, device fabrication and characterization; S2 X-ray Photoelectron Spectroscopy (XPS) and Energy-Filtered Photoemission of Electrons Microscopy (EF-PEEM); Computational procedure; Table S1 Effect of doping on CZTS photoemission properties and device performance; Fig. S1-S3 XPS spectra of non-doped, Sb-doped and Na:Sb-doped CZTS films.; Table S2 Metal ratios determined for non-doped and doped CZTS films from XPS before and after Ar plasma treatment; Figure S4 SIMS depth profile of Sb in Sb-doped CZTS film; Figure S5 Calculated partial density of states for Cu_2ZnSnS_4; Figure S6 Conductance maps for non-doped and doped CZTS films; Figure S7 Raman spectra and maps (A-mode) non-doped and doped CZTS films; Figure S8 Mott-Schottky plot for CdS films for determination of flat band potential.

Notes

The authors declare no competing financial interest.

Acknowledgement

DT and DJF are indebted to the Engineering and Physical Sciences Research Council (EPSRC) for supporting the work through PVTEAM grant (EP/L017792/1). MC and NAF acknowledge the support from EPSRC for the Bristol NanoESCA Facility under the strategic equipment panel (grants EP/K035746/1, EP/M000605/1). The authors are thankful to Dr. Benjamin Buse and Dr. Stuart Kearns from School of Earth Sciences (University of Bristol) for their support with WDS measurements, and to Dr. Peter Heard from Interface Analysis Centre (University of Bristol) for the SIMS measurements. The instrumentation for microscopy and impedance analysis is set up under the EPSRC's CDT Capital grant (EP/K035746/1). The

authors are also grateful to Helmholtz Zentrum für Materialien und Energie, Berlin, for their support and hospitality.

References

(1) Kim, J.; Hiroi, H.; Todorov, T. K.; Gunawan, O.; Kuwahara, M.; Gokmen, T.; Nair, D.; Hopstaken, M.; Shin, B.; Lee, Y. S.; et al. High Efficiency $Cu_2ZnSn(S,Se)_4$ Solar Cells by Applying a Double In_2S_3/CdS Emitter. *Adv. Mater.* **2014**, *26*, 7427–7431.

(2) Li, W.; Tan, J. M. R.; Leow, S. W.; Lie, S.; Magdassi, S.; Wong, L. H. Recent Progress in Solution-Processed Copper-Chalcogenide Thin-Film Solar Cells. *Energy Technol.* **2018**, *6*, 46–59.

(3) Haight, R.; Gershon, T.; Gunawan, O.; Antunez, P.; Bishop, D.; Lee, Y. S.; Gokmen, T.; Sardashti, K.; Chagarov, E.; Kummel, A. Industrial Perspectives on Earth Abundant, Multinary Thin Film Photovoltaics. *Semicond. Sci. Technol.* **2017**, *32*, 033004-1–17.

(4) Shin, D.; Saparov, B.; Mitzi, D. B. Defect Engineering in Multinary Earth-Abundant Chalcogenide Photovoltaic Materials. *Adv. Energy Mater.* **2017**, *7*, 1602366-1–29.

(5) Repins, I.; Vora, N.; Beall, C.; Wei, S.-H.; Yan, Y.; Romero, M.; Teeter, G.; Du, H.; To, B.; Young, M.; et al. Kesterites and Chalcopyrites: A Comparison of Close Cousins. *MRS Proc.* **2011**, *1324*, d17-1–12.

(6) Jackson, P.; Wuerz, R.; Hariskos, D.; Lotter, E.; Witte, W.; Powalla, M. Effects of Heavy Alkali Elements in $Cu(In,Ga)Se_2$ Solar Cells with Efficiencies up to 22.6%. *Phys. Status Solidi - Rapid Res. Lett.* **2016**, *10*, 583–586.

(7) Hiroi, H.; Iwata, Y.; Adachi, S.; Sugimoto, H.; Yamada, A. New World-Record Efficiency for Pure-Sulfide $Cu(In,Ga)S_2$ Thin-Film Solar Cell with Cd-Free Buffer Layer via KCN-Free Process. *IEEE J. Photovoltaics* **2016**, *6*, 760–763.

(8) Kim, K.; Kim, I.; Oh, Y.; Lee, D.; Woo, K.; Jeong, S.; Moon, J. Influence of Precursor Type on Non-Toxic Hybrid Inks for High-Efficiency Cu_2ZnSnS_4 Thin-Film Solar Cells. *Green Chem.* **2014**, *16*, 4323–4332.

(9) Yan, C.; Huang, J.; Sun, K.; Johnston, S.; Zhang, Y.; Sun, H.; Pu, A.; He, M.; Liu, F.; Eder, K.; et al. Cu_2ZnSnS_4 Solar Cells with over 10% Power Conversion Efficiency Enabled by Heterojunction Heat Treatment. *Nat. Energy* **2018**, *3*, 764–772.

(10) Antunez, P. D.; Bishop, D. M.; Lee, Y. S.; Gokmen, T.; Gunawan, O.; Gershon, T. S.; Todorov, T. K.; Singh, S.; Haight, R. Back Contact Engineering for Increased Performance in Kesterite Solar Cells. *Adv. Energy Mater.* **2017**, *7*, 1602585.

(11) Tiwari, D.; Skidchenko, E.; Bowers, J.; Yakushev, M. V.; Martin, R.; Fermin, D. J. Spectroscopic and Electrical Signatures of Acceptor States in Solution Processed $Cu_2ZnSn(S,Se)_4$ Solar Cells. *J. Mater. Chem. C* **2017**, *5*, 12720–12727.

(12) Bourdais, S.; Chone, C.; Delatouche, B.; Jacob, A.; Larramona, G.; Moisan, C.; Lafond, A.; Donatini, F.; Rey, G.; Siebentritt, S.; et al. Is the Cu/Zn Disorder the Main Culprit for the Voltage Deficit in Kesterite Solar Cells? *Adv. Energy Mater.* **2016**, *6*,

1502276-1–21.

(13) Park, J.-S.; Kim, S.; Walsh, A. Opposing Effects of Stacking Faults and Antisite Domain Boundaries on the Conduction Band Edge in Kesterite Quaternary Semiconductors. *Phys. Rev. Mater.* **2018**, *2*, 014602-1–5.

(14) Kim, S.; Park, J. S.; Walsh, A. Identification of Killer Defects in Kesterite Thin-Film Solar Cells. *ACS Energy Lett.* **2018**, *3*, 496–500.

(15) Kattan, N. A.; Griffiths, I. J.; Cherns, D.; Fermín, D. J. Observation of Antisite Domain Boundaries in Cu_2ZnSnS_4 by Atomic-Resolution Transmission Electron Microscopy. *Nanoscale* **2016**, *8*, 14369–14373.

(16) Valakh, M. Y.; Kolomys, O. F.; Ponomaryov, S. S.; Yukhymchuk, V. O.; Babichuk, I. S.; Izquierdo-Roca, V.; Saucedo, E.; Perez-Rodriguez, A.; Morante, J. R.; Schorr, S.; et al. Raman Scattering and Disorder Effect in Cu_2ZnSnS_4. *Phys. Status Solidi - Rapid Res. Lett.* **2013**, *7*, 258–261.

(17) Xie, H.; Sánchez, Y.; López-Marino, S.; Espíndola-Rodríguez, M.; Neuschitzer, M.; Sylla, D.; Fairbrother, A.; Izquierdo-Roca, V.; Pérez-Rodríguez, A.; Saucedo, E. Impact of Sn(S,Se) Secondary Phases in $Cu_2ZnSn(S,Se)_4$ Solar Cells: A Chemical Route for Their Selective Removal and Absorber Surface Passivation. *ACS Appl. Mater. Interfaces* **2014**, *6*, 12744–12751.

(18) Xie, H.; Dimitrievska, M.; Fontané, X.; Sánchez, Y.; López-Marino, S.; Izquierdo-Roca, V.; Bermúdez, V.; Pérez-Rodríguez, A.; Saucedo, E. Formation and Impact of Secondary Phases in Cu-Poor Zn-Rich $Cu_2ZnSn(S_{1-y}Se_y)_4$ ($0 \leq y \leq 1$) Based Solar Cells. *Sol. Energy Mater. Sol. Cells* **2015**, *140*, 289–298.

(19) Just, J.; Lützenkirchen-Hecht, D.; Frahm, R.; Schorr, S.; Unold, T. Determination of Secondary Phases in Kesterite Cu_2ZnSnS_4 Thin Films by x-Ray Absorption near Edge Structure Analysis. *Appl. Phys. Lett.* **2011**, *99*, 262105.

(20) Just, J.; Lützenkirchen-Hecht, D.; Müller, O.; Frahm, R.; Unold, T. Depth Distribution of Secondary Phases in Kesterite Cu_2ZnSnS_4 by Angle-Resolved X-Ray Absorption Spectroscopy. *APL Mater.* **2017**, *5*, 126106.

(21) Fontané, X.; Calvo-Barrio, L.; Izquierdo-Roca, V.; Saucedo, E.; Pérez-Rodriguez, A.; Morante, J. R.; Berg, D. M.; Dale, P. J.; Siebentritt, S. In-Depth Resolved Raman Scattering Analysis for the Identification of Secondary Phases: Characterization of Cu_2ZnSnS_4 Layers for Solar Cell Applications. *Appl. Phys. Lett.* **2011**, *98*, 181905.

(22) Paris, M.; Choubrac, L.; Lafond, A.; Guillot-Deudon, C.; Jobic, S. Solid-State NMR and Raman Spectroscopy to Address the Local Structure of Defects and the Tricky Issue of the Cu/Zn Disorder in Cu-Poor, Zn-Rich CZTS Materials. *Inorg. Chem.* **2014**, *53*, 8646–8653.

(23) Salomé, P. M. P.; Fernandes, P. A.; Leitão, J. P.; Sousa, M. G.; Teixeira, J. P.; Da Cunha, A. F. Secondary Crystalline Phases Identification in $Cu_2ZnSnSe_4$ Thin Films: Contributions from Raman Scattering and Photoluminescence. *J. Mater. Sci.* **2014**, *49*, 7425–7436.

(24) Davydova, A.; Rudisch, K.; Scragg, J. J. S. The Single Phase Region in Cu_2ZnSnS_4 Thin Films from Theory and Combinatorial Experiments. *Chem. Mater.* **2018**, *30*, 4624–4638.

(25) Johnson, M. C.; Wrasman, C.; Zhang, X.; Manno, M.; Leighton, C.; Aydil, E. S. Self-Regulation of Cu/Sn Ratio in the Synthesis of Cu_2ZnSnS_4 Films. *Chem. Mater.* **2015**, *27*, 2507–2514.

(26) Zhang, X.; Han, M.; Zeng, Z.; Duan, Y. The Role of Sb in Solar Cell Material Cu_2ZnSnS_4. *J. Mater. Chem. A* **2017**, *5*, 6606–6612.

(27) Yan, C.; Sun, K.; Huang, J.; Johnston, S.; Liu, F.; Veettil, B. P.; Sun, K.; Pu, A.; Zhou, F.; Stride, J. A.; et al. Beyond 11% Efficient Sulfide Kesterite $Cu_2Zn_xCd_{1-x}SnS_4$ Solar Cell: Effects of Cadmium Alloying. *ACS Energy Lett.* **2017**, *2*, 930–936.

(28) Tiwari, D.; Koehler, T.; Lin, X.; Harniman, R.; Griffiths, I.; Wang, L.; Cherns, D.; Klenk, R.; Fermin, D. J. Cu_2ZnSnS_4 Thin Films Generated from a Single Solution Based Precursor: The Effect of Na and Sb Doping. *Chem. Mater.* **2016**, *28*, 4991–4997.

(29) Xiao, W.; Wang, J. N.; Zhao, X. S.; Wang, J. W.; Huang, G. J.; Cheng, L.; Jiang, L. J.; Wang, L. G. Intrinsic Defects and Na Doping in Cu_2ZnSnS_4: A Density-Functional Theory Study. *Sol. Energy* **2015**, *116*, 125–132.

(30) Su, Z.; Tan, J. M. R.; Li, X.; Zeng, X.; Batabyal, S. K.; Wong, L. H. Cation Substitution of Solution-Processed Cu_2ZnSnS_4 Thin Film Solar Cell with over 9% Efficiency. *Adv. Energy Mater.* **2015**, *5*, 1500682–1500687.

(31) Qi, Y. F.; Kou, D. X.; Zhou, W. H.; Zhou, Z. J.; Tian, Q. W.; Meng, Y. N.; Liu, X. S.; Du, Z. L.; Wu, S. X. Engineering of Interface Band Bending and Defects Elimination via a Ag-Graded Active Layer for Efficient $(Cu,Ag)_2ZnSn(S,Se)_4$ Solar Cells. *Energy Environ. Sci.* **2017**, *10*, 2401–2410.

(32) Sai Gautam, G.; Senftle, T. P.; Carter, E. A. Understanding the Effects of Cd and Ag Doping in Cu_2ZnSnS_4 Solar Cells. *Chem. Mater.* **2018**, *30*, 4543–4555.

(33) Nagaoka, A.; Miyake, H.; Taniyama, T.; Kakimoto, K.; Nose, Y.; Scarpulla, M. A.; Yoshino, K. Effects of Sodium on Electrical Properties in Cu_2ZnSnS_4 Single Crystal. *Appl. Phys. Lett.* **2014**, *104*, 152101-1–4.

(34) Johnson, M.; Baryshev, S. V; Thimsen, E.; Manno, M.; Zhang, X.; Veryovkin, I. V; Leighton, C.; Aydil, E. S. Alkali-Metal-Enhanced Grain Growth in Cu_2ZnSnS_4 Thin Films. *Energy Environ. Sci.* **2014**, *7*, 1931–1938.

(35) Giraldo, S.; Saucedo, E.; Neuschitzer, M.; Oliva, F.; Placidi, M.; Alcobé, X.; Izquierdo-Roca, V.; Kim, S.; Tampo, H.; Shibata, H.; et al. How Small Amounts of Ge Modify the Formation Pathways and Crystallization of Kesterites. *Energy Environ. Sci.* **2018**, *11*, 582–593.

(36) Troviano, M.; Taretto, K. Analysis of Internal Quantum Efficiency in Double-Graded Bandgap Solar Cells Including Sub-Bandgap Absorption. *Sol. Energy Mater. Sol. Cells* **2011**, *95*, 821–828.

(37) Liu, X.; Feng, Y.; Cui, H.; Liu, F.; Hao, X.; Conibeer, G. The Current Status and Future Prospects of Kesterite Solar Cells: A Brief Review. *Prog. Photovoltaics Res. Appl.* **2016**, *24*, 879–898.

(38) Yuan, M.; Mitzi, D. B.; Liu, W.; Kellock, A. J.; Chey, S. J.; Deline, V. R. Optimization of CIGS-Based PV Device through Antimony Doping. *Chem. Mater.* **2010**, *22*, 285–287.

(39) Cahen, D.; Kahn, A. Electron Energetics at Surfaces and Interfaces: Concepts and Experiments. *Adv. Mater.* **2003**, *15*, 271–277.

(40) Escher, M.; Weber, N.; Merkel, M.; Ziethen, C.; Bernhard, P.; Schönhense, G.; Schmidt, S.; Forster, F.; Reinert, F.; Krömker, B.; et al. Nanoelectron Spectroscopy for Chemical Analysis: A Novel Energy Filter for Imaging x-Ray Photoemission Spectroscopy. *J. Phys. Condens. Matter* **2005**, *17*, S1329–S1338.

(41) Pandiyan, R.; Oulad Elhmaidi, Z.; Sekkat, Z.; Abd-lefdil, M.; El Khakani, M. A. Reconstructing the Energy Band Electronic Structure of Pulsed Laser Deposited CZTS Thin Films Intended for Solar Cell Absorber Applications. *Appl. Surf. Sci.* **2017**, *396*, 1562–1570.

(42) Kim, G. Y.; Son, D.-H.; Thi Thu Nguyen, T.; Yoon, S.; Kwon, M.; Jeon, C.-W.; Kim, D.-H.; Kang, J.-K.; Jo, W. Enhancement of Photo-Conversion Efficiency in $Cu_2ZnSn(S,Se)_4$ Thin-Film Solar Cells by Control of ZnS Precursor-Layer Thickness. *Prog. Photovolt Res. Appl.* **2016**, *24*, 292–306.

(43) Ettema, A. R. H. F.; De Groot, R. A.; Haas, C.; Turner, T. S. Electronic Structure of SnS Deduced from Photoelectron Spectra and Band-Structure Calculations. *Phys. Rev. B* **1992**, *46*, 7363–7373.

(44) Wang, S. F.; Wang, W.; Fong, W. K.; Yu, Y.; Surya, C. Tin Compensation for the SnS Based Optoelectronic Devices. *Sci. Rep.* **2017**, *7*, 39704-1–10.

(45) Tiwari, D.; Cattelan, M.; Harniman, R. L.; Sarua, A.; Abbas, A.; Bowers, J. W.; Fox, N. A.; Fermin, D. J. Mapping Shunting Paths at the Surface of $Cu_2ZnSn(S,Se)_4$ Films via Energy-Filtered Photoemission Microscopy. *iScience* **2018**, *9*, 36–46.

(46) Chen, J.; Shen, H.; Zhai, Z.; Li, Y.; Yi, Y. Performance Enhancement in Sb Doped $Cu(In,Ga)Se_2$ Thin Film Solar Cell by e-Beam Evaporation. *Appl. Surf. Sci.* **2018**, *433*, 271–278.

(47) Sun, Y.; Lin, S.; Li, W.; Cheng, S.; Zhang, Y.; Liu, Y.; Liu, W. Review on Alkali Element Doping in $Cu(In,Ga)Se_2$ Thin Films and Solar Cells. *Engineering* **2017**, *3*, 452–459.

(48) Scheer, R. Activation Energy of Heterojunction Diode Currents in the Limit of Interface Recombination. *J. Appl. Phys.* **2009**, *105*, 104505-1–6.

(49) Nakada, T. Nano-Structural Investigations on Cd-Doping into $Cu(In,Ga)Se_2$ Thin Films by Chemical Bath Deposition Process. *Thin Solid Films* **2000**, *362*, 346–352.

(50) Heske, C.; Eich, D.; Fink, R.; Umbach, E.; Van Buuren, T.; Bostedt, C.; Terminello, L. J.; Kakar, S.; Grush, M. M.; Callcott, T. A.; et al. Observation of Intermixing at the Buried $CdS/Cu(In,Ga)Se_2$ Thin Film Solar Cell Heterojunction. *Appl. Phys. Lett.* **1999**, *74*, 1451–1453.

(51) Bär, M.; Repins, I.; Weinhardt, L.; Alsmeier, J.-H.; Pookpanratana, S.; Blum, M.; Yang, W.; Heske, C.; Wilks, R. G.; Noufi, R. Zn–Se–Cd–S Interlayer Formation at the $CdS/Cu_2ZnSnSe_4$ Thin-Film Solar Cell Interface. *ACS Energy Lett.* **2017**, *2*, 1632–1640.